

Supplemental Material

Evaluation of shell preservation

Scanning Electron Microscopy (SEM)

Samples analyzed at the University of Alabama (UA) were evaluated for diagenesis using SEM evaluation of shell microstructure. A preservation index ranking system for preservation quality was developed for the crystal structures found in several shell layers of *Lahillia larseni* (Figs. S1 & S2) based on previously developed systems (Cochran et al., 2010; Knoll et al., 2016). Good preservation was inferred from observation of well-defined crystal boundaries and a lack of dissolution, overgrowth, or recrystallization features. Most shells exhibited good to excellent preservation and only 2 of 20 were discarded due to poorly-preserved microstructures (Figs. S3 & S4). Supplementary Figures S1 and S2 illustrate the Preservation Index (PI) ranking scales developed for four microstructures of *L. larseni* shells. These PI scales were modeled after those produced by Cochran et al. (2010) and Knoll et al. (2016), and were used to evaluate the quality of preservation of *L. larseni* shells in this study.

Supplementary Figures S3 and S4 present SEM images of *L. larseni* shells evaluated for preservational quality. Shells were ranked on a scale of 1 to 5, with 5 being perfectly preserved. Isotopic data from shells that received a score lower than 2.5 were excluded from summary figures (including main text Figure 2). In figures S3 and S4, two SEM images are included for each *L. larseni* shell, with the image on the left representing some of the highest quality microstructural preservation observed within the shell, and the image on the right representative of some of the lowest quality microstructural preservation observed. The final PI score assigned to each shell (listed in parentheses after the shell's ID number in Figures S3 and S4) reflects the relative proportion of well-preserved and poorly-preserved areas within the shells, and places more weight on microstructures commonly found in the region of the shell that was sampled for isotopic analysis.

The exterior portions of the shell typically targeted for isotopic analysis generally consist of the branching crossed-lamellar (BCL), crossed-lamellar (CL), and to a lesser extent, crossed-lamellar/crossed acicular (CL/CA) microstructures (Figs. S1 & S2). The cone complex crossed-lamellar (Cone CCL) microstructure is found in the most interior part of the shell (Fig. S2). SEM evaluation consisted of an examination of a full vertical cross-section of the shell, from the exterior-most to the interior-most shell layer. All microstructures present were evaluated, but greater emphasis was placed on the exterior-most microstructures when determining the PI score assigned to any given shell in order to conservatively score shells that may have been affected by surficial alteration. However, in general, the quality of preservation was fairly consistent between all shell layers (internal and external) for any given shell.

Other methods

All samples analyzed at the University of Michigan (UM) were assessed for diagenetic alteration using similar methods. The mineralogy was evaluated using X-ray diffraction (XRD) to determine whether original aragonitic mineralogy was preserved. Since some recrystallization

to calcite can occur below XRD detection limits, thick and thin sections were also evaluated with cathodoluminescence (CL) microscopy. CL microscopy detects elevated concentrations of ions such as Mn^{2+} , which generally indicate areas of diagenetic alteration. Almost all shells were non-luminescent except in rare cases along fractures – these areas were avoided during sampling. Finally, powdered sample material from multiple locations on each shell was analyzed for trace element concentration to examine [Mn], [Fe], and [Sr], as mollusks are known to have natural concentrations of these elements and deviations from these limits can indicate post burial diagenesis (Morrison and Brand, 1986; Brand and Morrison, 1987). Approximately 10% of samples were eliminated under trace element criteria.

Isotopic methods

Samples and standards (NBS-19) analyzed at UA were acidified at 50 °C in a Thermo GasBench II connected via continuous flow to a Thermo Delta V Plus Mass Spectrometer, following the methods of Ellis and Tobin (2019) at the Alabama Stable Isotope Laboratory (ASIL). Typical analytical precision was $\pm 0.08\text{‰}$ for $\delta^{18}\text{O}$ and $\pm 0.04\text{‰}$ for $\delta^{13}\text{C}$. Samples and standards (NBS-19) analyzed at UM from Dutton (2003) were generated using a Finnigan MAT 251 IRMS coupled with an automated Kiel Device. These samples were first roasted *in vacuo* at 200 °C to remove volatile contaminants. Samples and standards (NBS-18, 19) measured at UM as part of this study were not roasted, and were analyzed with Thermo MAT 253 IRMS, also coupled to a Kiel Device.

Comparison of temperatures calculated from constant or fluctuating $\delta^{18}\text{O}_w$ values

Petersen et al. (2016) presented calculated seawater $\delta^{18}\text{O}$ ($\delta^{18}\text{O}_w$) values across the latest Cretaceous and early Paleogene at our study site, demonstrating that the $\delta^{18}\text{O}_w$ values were not constant throughout that interval. The supplementary data from Petersen et al. (2016) provides calculated $\delta^{18}\text{O}_w$ values at intermittent discrete stratigraphic heights from 400 m below the K-Pg boundary to 39 m above the K-Pg boundary. We calculated temperatures from our stratigraphic oxygen isotope data (Text Fig. 2) in two different ways: first, assuming that $\delta^{18}\text{O}_w$ values were a constant -1.2‰ ; and second, incorporating the fluctuating $\delta^{18}\text{O}_w$ values from Petersen et al. (2016). The paleotemperature equation of Kim et al. (2007) was used to calculate temperatures.

Because there is not a reported $\delta^{18}\text{O}_w$ value for every stratigraphic horizon at which our sampled shells are positioned, it was necessary to produce a linear interpolation of $\delta^{18}\text{O}_w$ values so that an estimate of $\delta^{18}\text{O}_w$ was available for each stratigraphic height at which we sampled. There are obvious concerns with using linear interpolation, as we cannot necessarily assume that $\delta^{18}\text{O}_w$ fluctuations followed linear trends. The stratigraphic range of our samples (>60 m above the K-Pg) also exceeded the range for which $\delta^{18}\text{O}_w$ values have been reported (up to 39 m above the K-Pg), making it difficult to estimate $\delta^{18}\text{O}_w$ without making assumptions regarding extrapolation. We used the $\delta^{18}\text{O}_w$ value reported for 39 m above the K-Pg for all stratigraphic heights above that point.

The results of our comparisons are presented in Supplementary Figure S7. Panel A is the stratigraphic carbon isotope data (the same data presented in Text Fig. 2). Panel B is the stratigraphic oxygen isotope data (from Text Fig. 2), converted to temperature values assuming a

constant $\delta^{18}\text{O}_w$ value of -1.2‰ through the whole section. Horizontal range bars depict the total range of calculated temperature values recorded in each individual shell. Panel C is the stratigraphic oxygen isotope data (from Text Fig. 2), converted to temperature values using the linearly-interpolated $\delta^{18}\text{O}_w$ values from Petersen et al. (2016). Again, horizontal range bars depict the total range of calculated temperature values within each individual shell. Panel D is the same as Panel C, but horizontal range bars now incorporate the largest possible temperature range based on a linear interpolation of the minimum and maximum $\delta^{18}\text{O}_w$ values reported by Petersen et al. (2016) at each horizon (For Panel C, the linear interpolation was based on the average $\delta^{18}\text{O}_w$ value reported by Petersen et al. (2016) at each horizon).

Comparing Panels B and C in Supplementary Figure S7, we do not see enough significant differences to warrant concern over assuming a constant $\delta^{18}\text{O}_w$ value for the entire section. Panel C does show some warmer temperatures than Panel B ~150m below the K-Pg boundary, but in the vicinity of the two intervals (Ints. I and II) we define and discuss in the text, the incorporation of the fluctuating $\delta^{18}\text{O}_w$ values compared to a constant $\delta^{18}\text{O}_w$ value does not alter our interpretation of events.

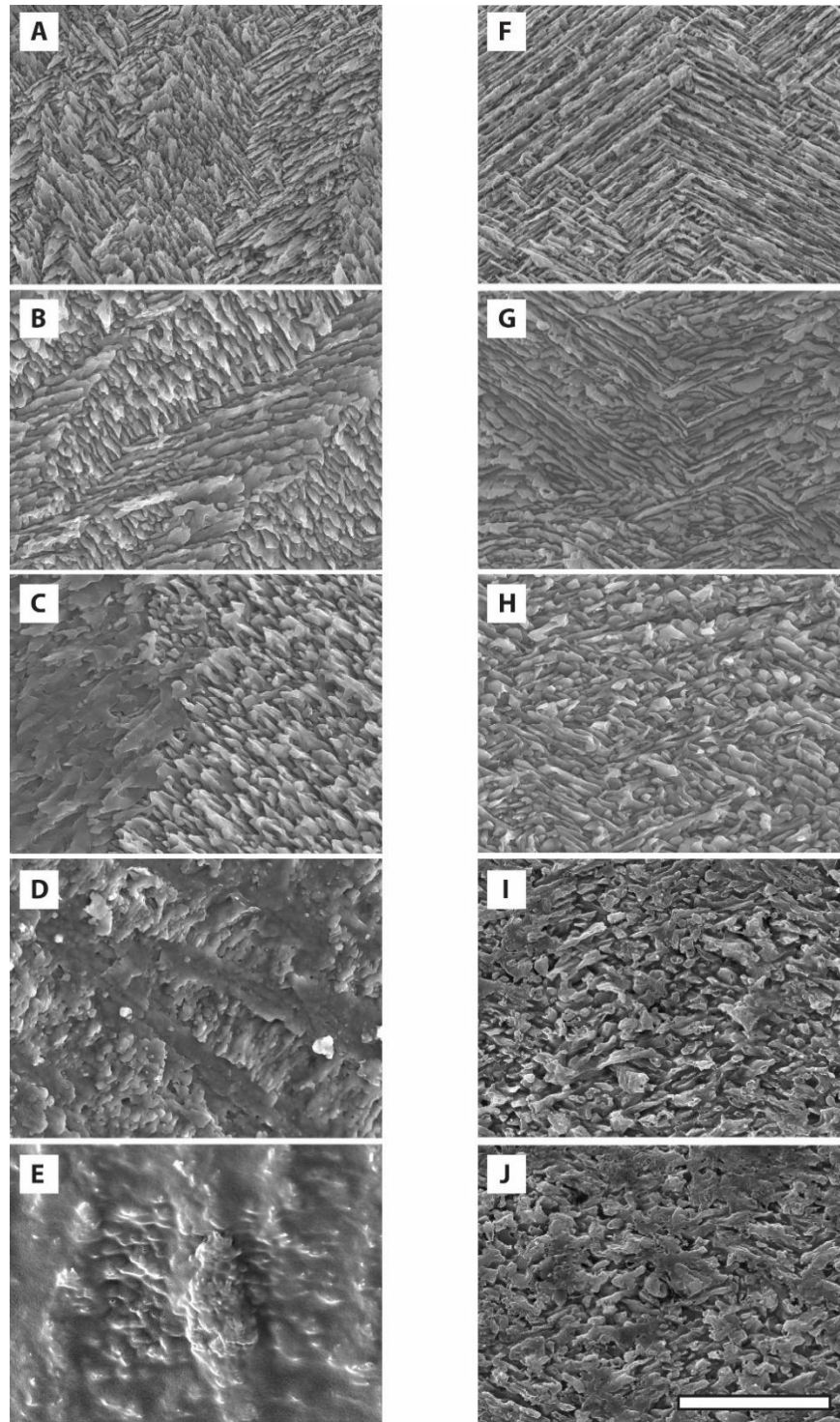
Impact of *L. larseni* sampling strategies on isotopic data

Of the 16 shells sampled at high (subannual) resolution, five were sampled at the University of Michigan (see Supplementary Table S1) and targeted the ventral margin or the hinge of the shells. The rest of the high-resolution sampling was conducted at the University of Alabama, where sampling typically targeted the middle of the valve (see Fig. S5). Three of these shells sampled at high subannual resolution were sampled in more than one ontogenetic position (umbo, mid-shell, and/or ventral margin). Additionally, the five low-resolution shells sampled at the University of Michigan were sampled along the entire growth axis of the shell, from umbo to ventral margin using a larger spot size. Estimates of *L. larseni* lifespan range between 42 and 58 years (n=2; Moss et al., 2017).

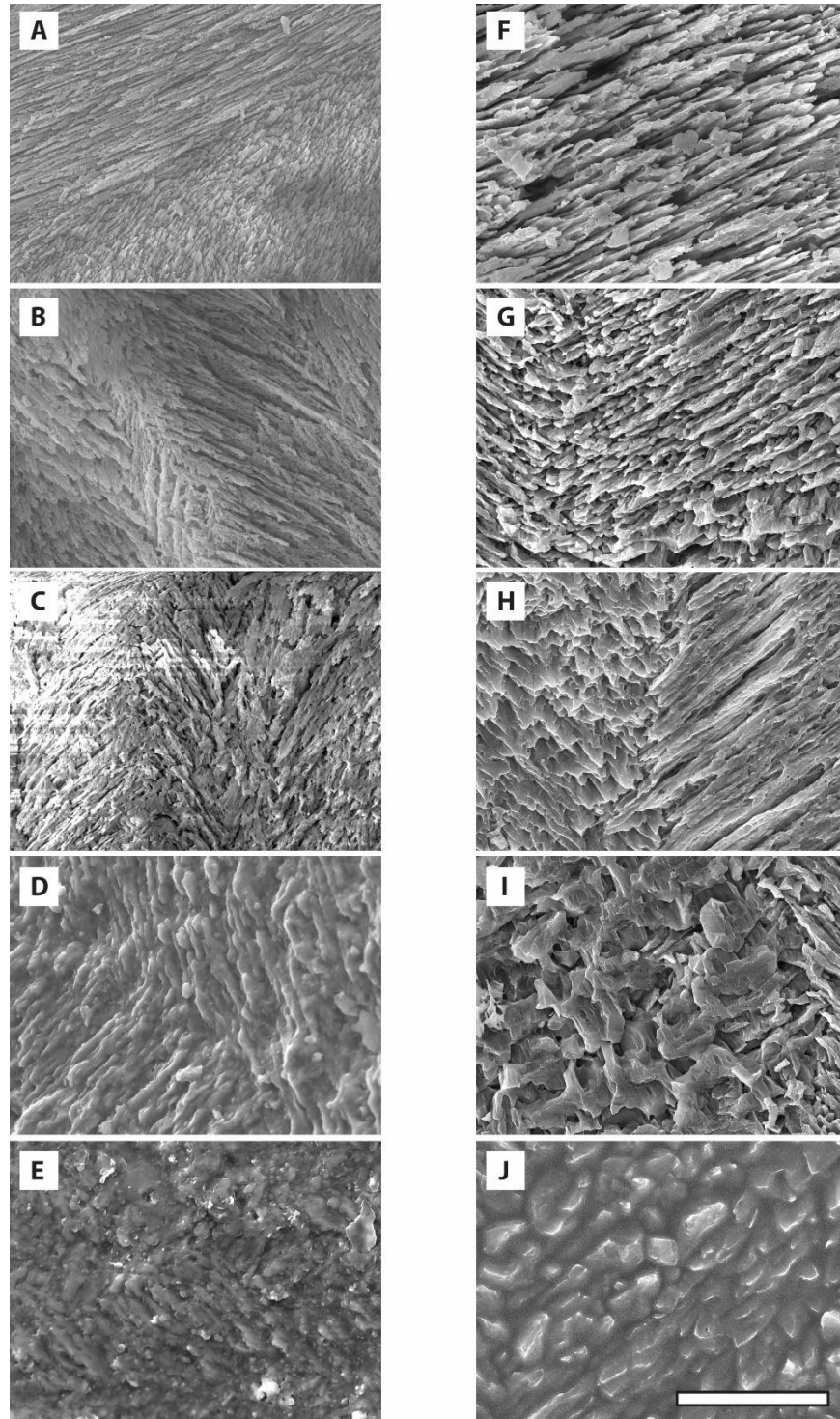
Most of the shells sampled at multiple ontogenetic positions are represented by our low-resolution sampling strategy. To assess the impact that the low-resolution sampling had on our stratigraphic isotope trends, we compared our stratigraphic plot from Figure 2 with and without low-resolution sampled shells (Figure S9). In either case (Fig. S9 part A or B), the LOESS curves indicate decreases in average $\delta^{13}\text{C}$ or $\delta^{18}\text{O}$ values within our defined intervals I and II, meaning that our overall interpretation remains the same whether or not low-resolution sampled shells are included in the dataset. Figure S9 demonstrates that stratigraphic trends in isotope values are not an artifact of inadvertently sampling different ontogenetic stages of *L. larseni* shells, and that our interpretations of stratigraphic trends are insensitive to the exact position of sampling on the shell.

Shell ID	Stratigraphic Height to KPB (m)	Stable Isotope Analysis					Evaluation of Shell Preservation		
		Sampling Location				Sampling Resolution	Analyzed at?	Method	Analyzed at?
		H	U	M	V				
UWBM-109964	65			X		high	UA	SEM	UA
UWBM-109963	56.6			X		low	UA	SEM	UA
UWBM-109962	46			X		high	UA	SEM	UA
L1430A1	40	X				high	UM(Dutton)	Trace element	P2016
UWBM-109960	35.4			X		low	UA	SEM	UA
UWBM-109961	35.4			X		low	UA	SEM	UA
UWBM-109959	26.4			X		low	UA	SEM	UA
UWBM-109958	15.7			X		high	UA	SEM	UA
UWBM-107333	4.8			X		low	UA	SEM	UA
UWBM-109955	1.5			X		high	UA	SEM	UA
UWBM-109956	1.5		X	X		low	UA	SEM	UA
UWBM-109957	1.5			X		high	UA	SEM	UA
L1529A	1				X	high	UM(Dutton)	Trace element	P2016
L447D	0		X	X	X	low	UM(Oliphant)	Trace element	P2016
UWBM-109954	-0.3			X		high	UA	SEM	UA
UWBM-107332	-1.6		X	X	X	low	UA	SEM	UA
UWBM-107343	-4.2			X		high	UA	SEM	UA
L1161	-7		X	X	X	low	UM(Oliphant)	Trace element	P2016
UWBM-109951	-35			X	X	high	UA	SEM	UA
UWBM-109952	-35			X	X	high	UA	SEM	UA
UWBM-109953	-35			X		high	UA	SEM	UA
L1474A	-42		X	X	X	low	UM(Oliphant)	Trace element	P2016
UWBM-107338	-84			X		low	UA	SEM	UA
L1480E	-85	X				high	UM(Dutton)	Trace element	P2016
L1480B	-85	X				high	UM(Dutton)	Trace element	P2016
UWBM-107339	-87.6			X		low	UA	SEM	UA
UWBM-107335	-91.1			X		high	UA	SEM	UA
L757b	-133				X	high	UM(Dutton)	Trace element	P2016
L1609	-171		X	X	X	low	UM(Oliphant)	Trace element	P2016
L776A	-233		X	X	X	low	UM(Oliphant)	Trace element	P2016

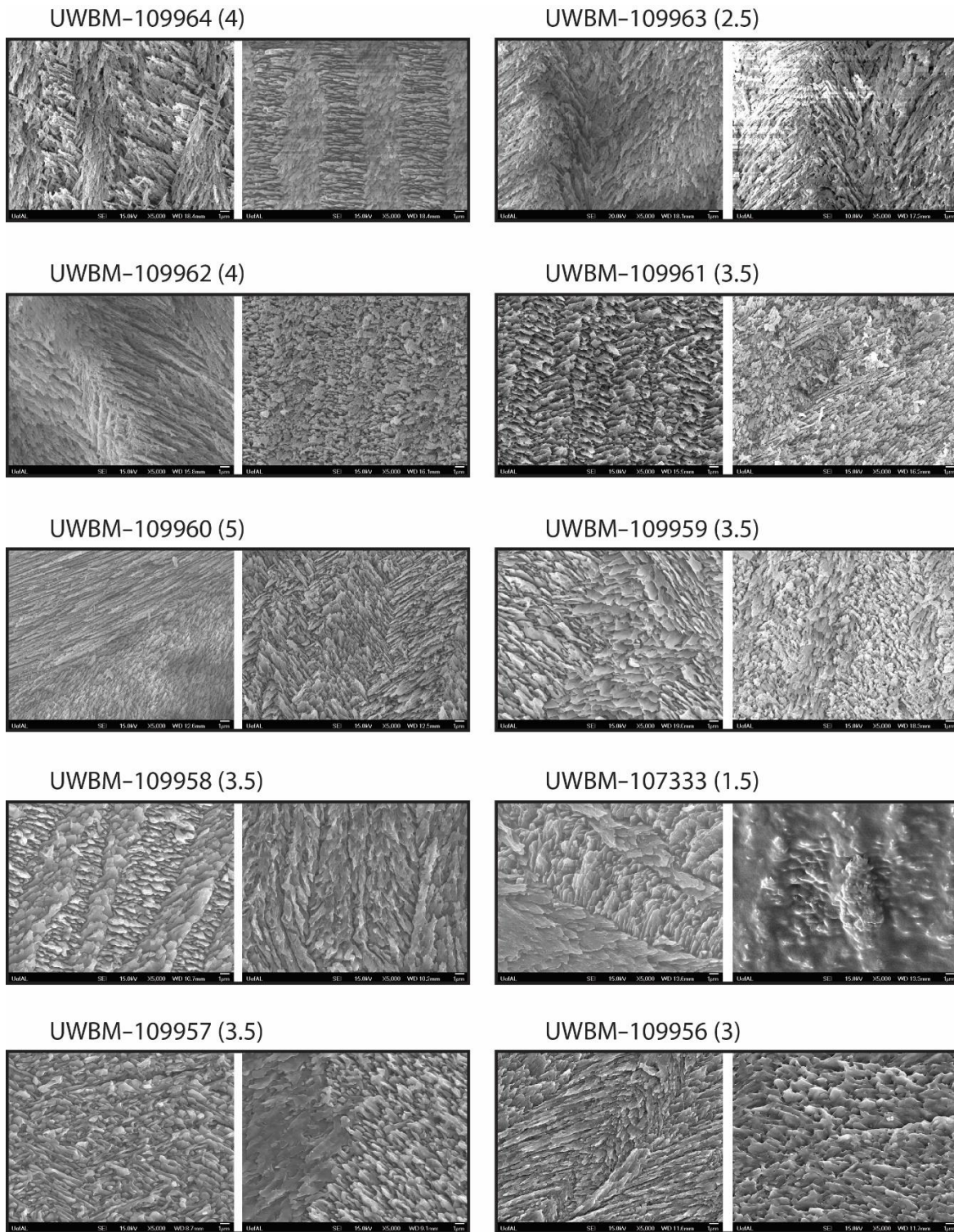
Supplementary Table S1. A summary of the isotope sampling resolution (high/subannual vs. low), isotope analysis method (UM or UA lab protocols, see ‘Isotopic methods’ supplementary section above), and preservation evaluation method for each sampled *L. larseni* shell. Sampling locations are as follows: H-hinge, U-umbo, M-middle of valve, V-ventral margin. For trace element analyses, “P2016” indicates shells evaluated previously for diagenetic alteration, with trace element concentrations reported in Petersen et al. (2016).



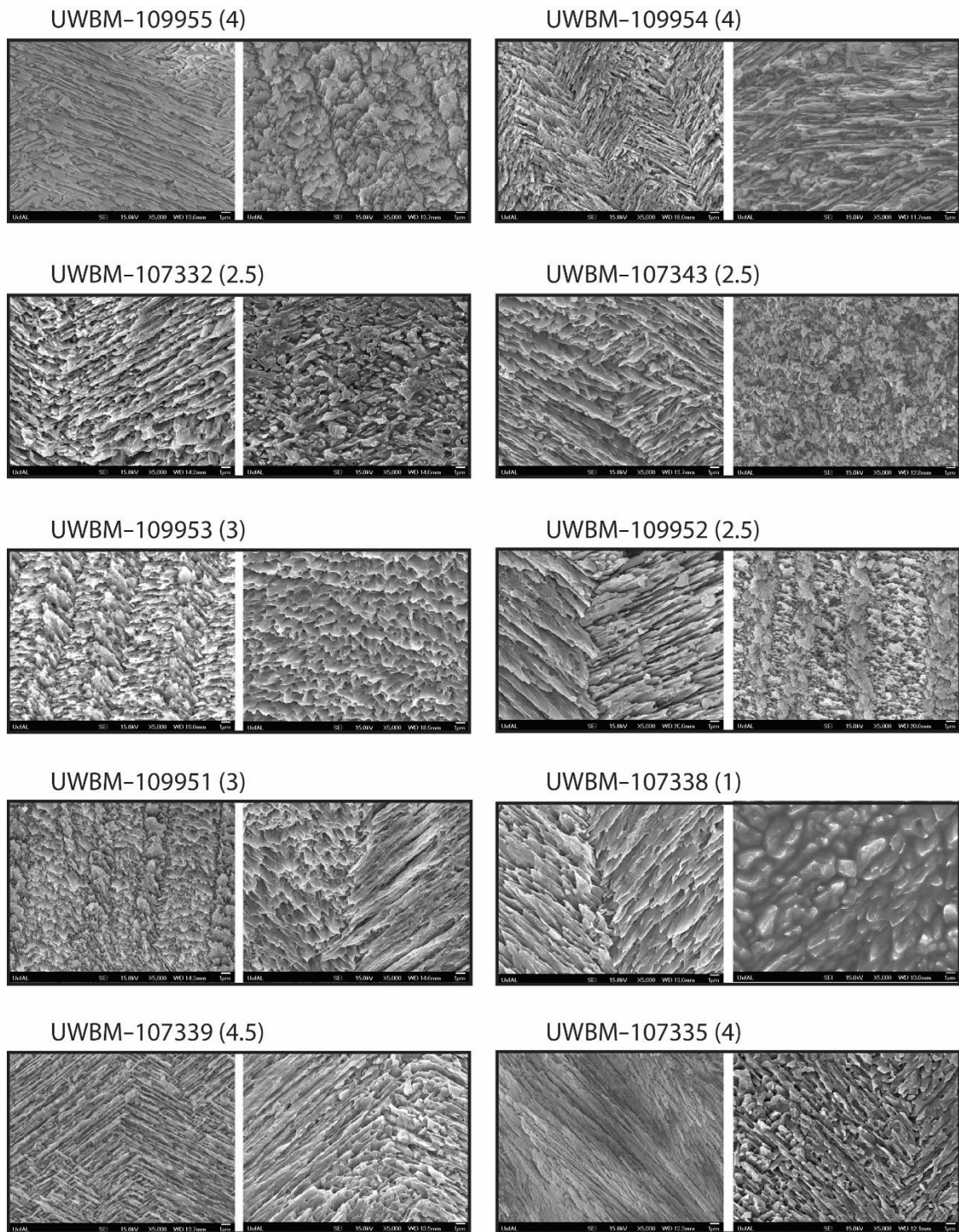
Supplementary Figure S1. SEM images illustrating PI scales for the branching crossed-lamellar (BCL) and transitional crossed-lamellar crossed-acicular (CL/CA) microstructures found in *L. larseni* shells. All images taken at $\times 5,000$ magnification. Scale bar represents $10\ \mu\text{m}$. A-E) PI scale for the BCL microstructure, with A representing the best possible score of 5 and E representing the lowest score of 1. F-J) PI scale for the CL/CA microstructure, with F representing the highest score of 5 and J representing the lowest score of 1.



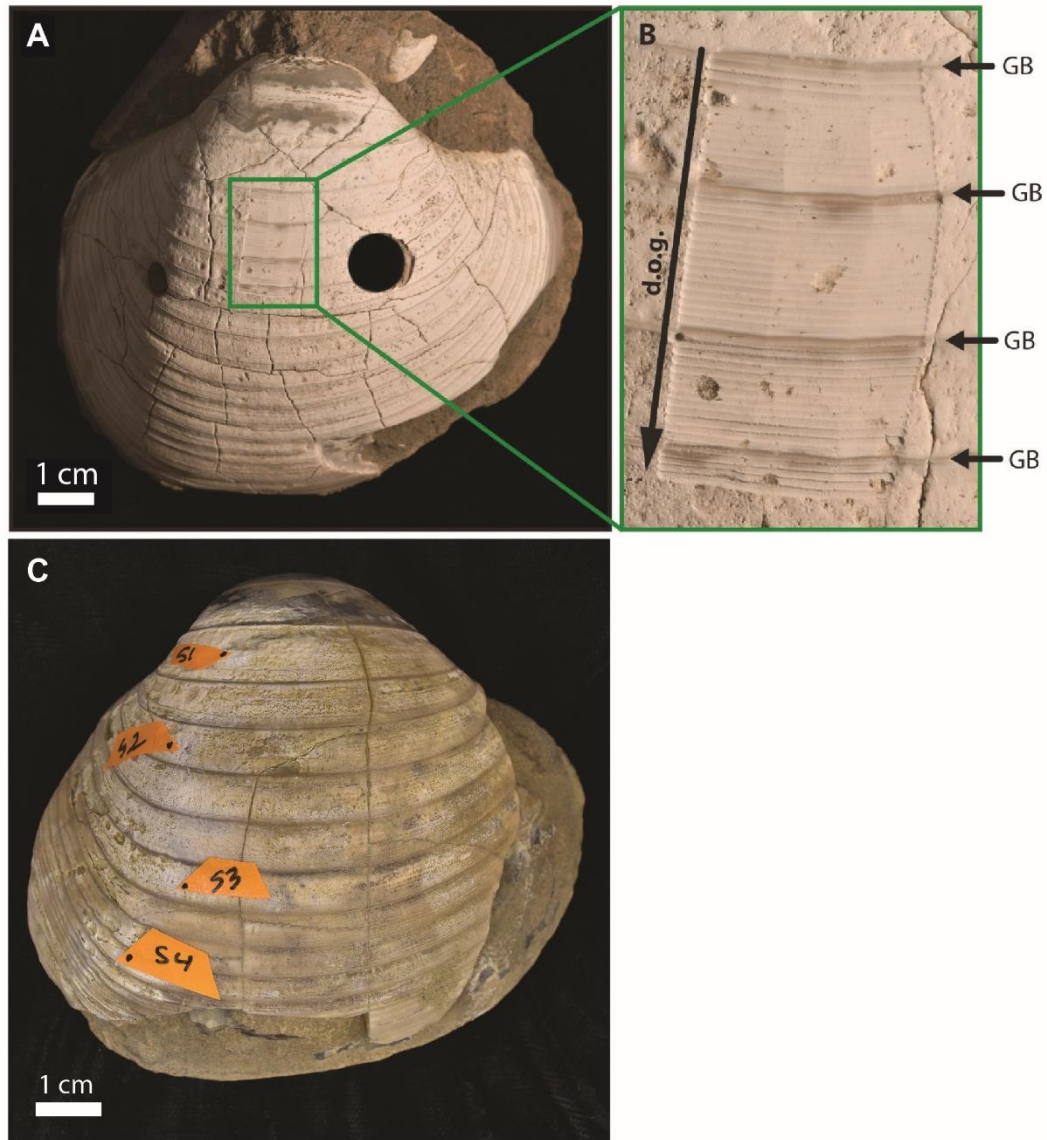
Supplementary Figure S2. SEM images illustrating PI scales for the crossed-lamellar (CL) and cone complex crossed-lamellar (Cone CCL) microstructures found in *L. larseni* shells. All images taken at $\times 5,000$ magnification. Scale bar represents 10 μm . A-E) PI scale for the CL microstructure, with A representing the best possible score of 5 and E representing the lowest score of 1. F-J) PI scale for the Cone CCL microstructure, with F representing the highest score of 5 and J representing the lowest score of 1.



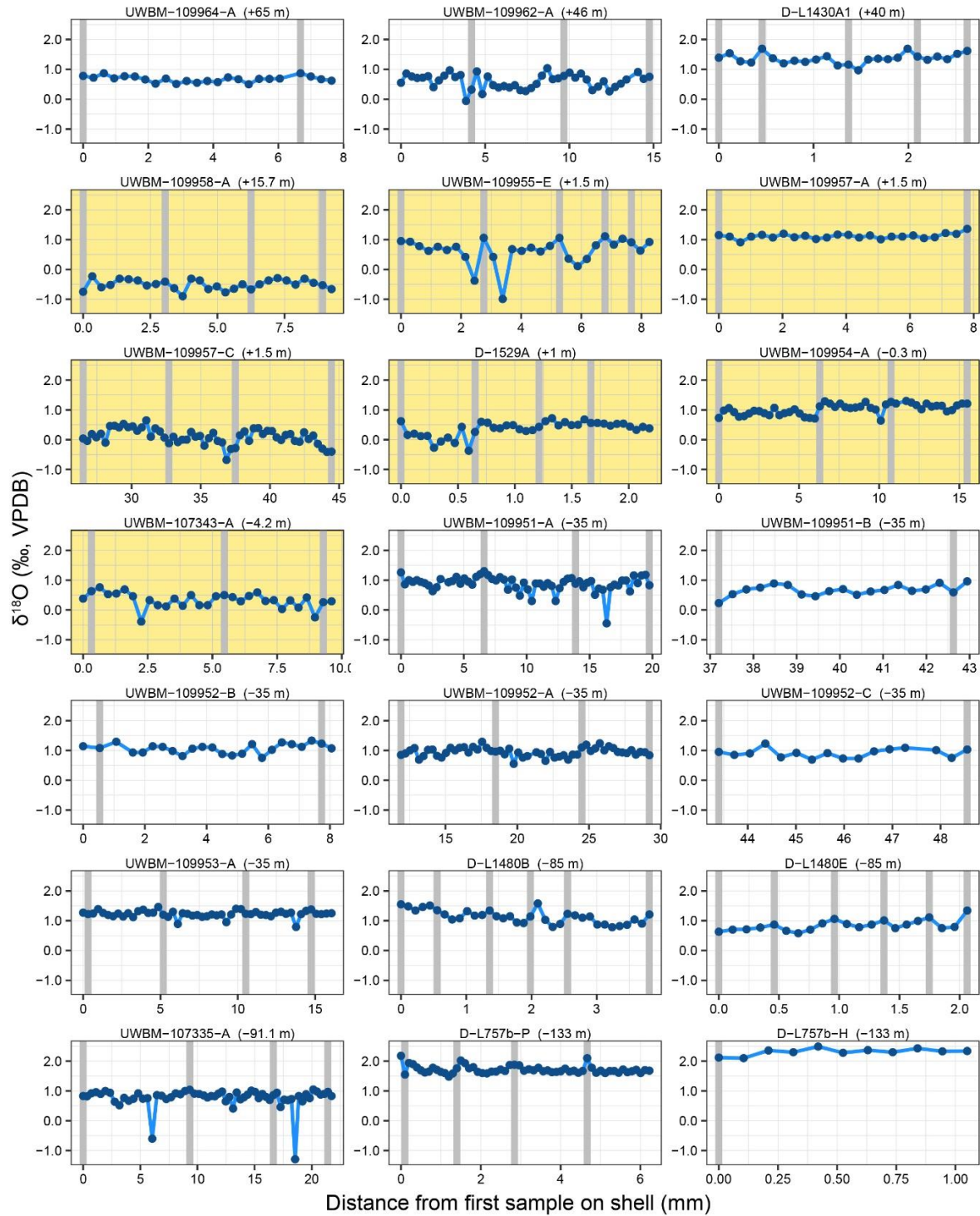
Supplementary Figure S3. SEM images from the first 10 of 20 *L. larseni* shells evaluated for diagenesis using the developed PI scales. Two images are present for each shell, with the left image representing the most well-preserved area and the right image representing the most poorly-preserved area. The PI score assigned to each shell is listed in parentheses following the shell's ID.



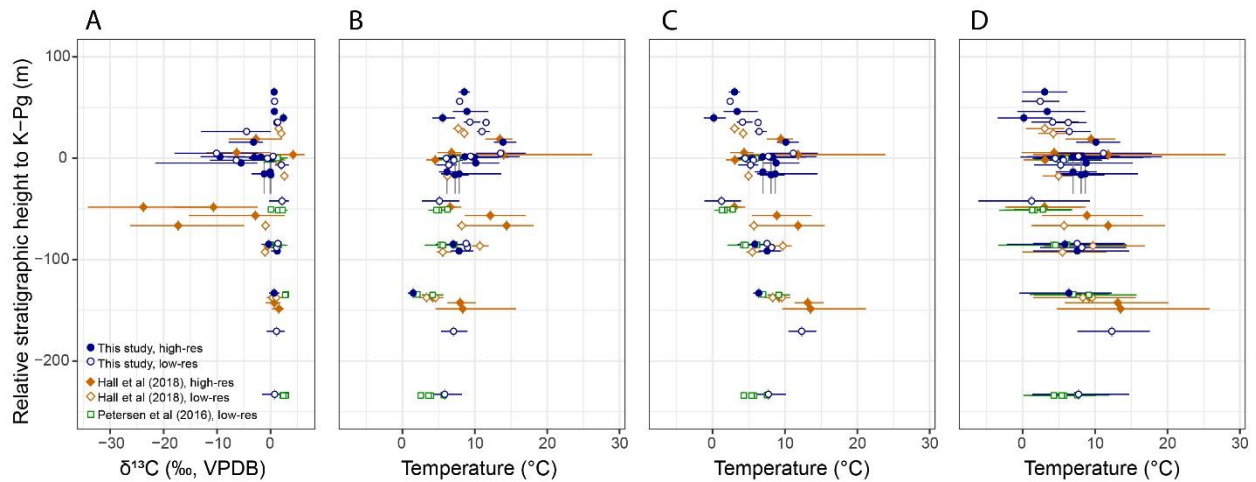
Supplementary Figure S4. SEM images from 10 of 20 *L. larseni* shells evaluated for diagenesis using the developed PI scales. Two images are present for each shell, with the left image representing the most well-preserved area and the right image representing the most poorly-preserved area. The PI score assigned to each shell is listed in parentheses following the shell's ID.



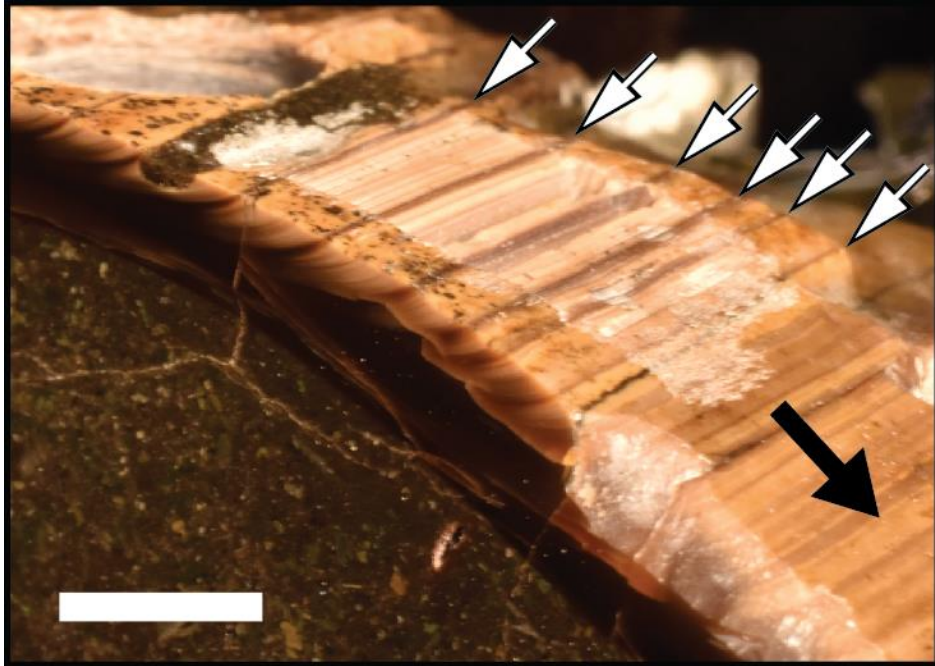
Supplementary Figure S5. Images illustrating the sampling strategies used for both high- and low-resolution ontogenetic sampling of *L. larseni* shells for isotopic analysis. A) Specimen of *L. larseni* (UWBM-109953) sampled at high-resolution with the micromill. The micromilled region is outlined in green, and the hole to the right indicates where shell was removed for preservational evaluation via SEM. B) Micromilled region of UWBM-109953 is shown in detail, with arrows indicating the direction of growth (d.o.g.) and the location of dark growth bands (GB) found at the end of each growth increment. C) Specimen of *L. larseni* (UWBM-109956) sampled at low-resolution with a hand drill. Black dots on the orange labels indicate locations where sampling occurred.



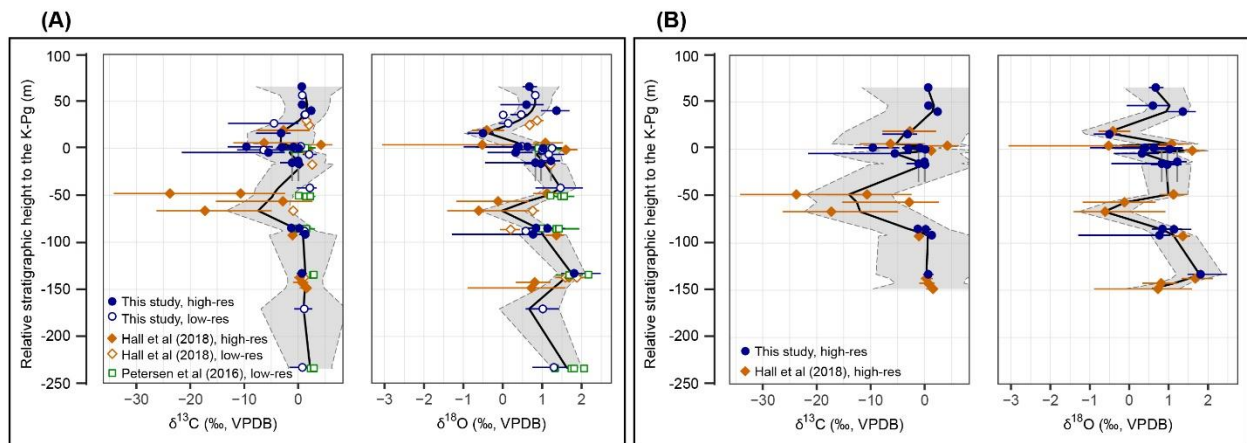
Supplementary Figure S6. Ontogenetic oxygen isotope profiles of *Lahillia larseni* shells sampled at high (subannual) resolution, labeled with profile ID and stratigraphic height of the sample in meters relative to the K-Pg boundary. Vertical grey bars indicate locations of visually-distinct dark growth bands separating annual growth increments. Direction of growth is from left to right in all plots. Samples occurring within Interval II are highlighted with a yellow background.



Supplementary Figure S7. A comparison of stratigraphic trends in temperature from *L. larseni* shells calculated using either constant or fluctuating $\delta^{18}\text{O}_w$ values. A) Stratigraphic plot of carbon isotope data. B) Stratigraphic temperature plot with temperatures calculated using a constant $\delta^{18}\text{O}_w$ value of -1.2‰ . C) Stratigraphic temperature plot with temperatures calculated using fluctuating $\delta^{18}\text{O}_w$ values linearly interpolated from Petersen et al. (2016). Range bars reflect the variation of $\delta^{18}\text{O}$ within each individual shell. D) Same plot as panel C, but range bars now reflect both the variation of $\delta^{18}\text{O}$ within each individual shell and the range of reported $\delta^{18}\text{O}_w$ for each horizon, determined by linearly interpolating reported maximum and minimum $\delta^{18}\text{O}_w$ values from Petersen et al. (2016) instead of average reported $\delta^{18}\text{O}_w$ values as used in panel C.



Supplementary Figure S8. Oblique view of sectioned *L. larseni* shell showing the relationship between dark growth bands visible on the exterior of the shell and dark growth bands visible in cross-section. White arrows point to dark growth bands on the exterior surface of the shell. Black arrow in lower right corner indicates direction of growth. White scale bar represents 5 mm.



Supplementary Figure S9. Comparison of stratigraphic isotope ($\delta^{13}\text{C}$ and $\delta^{18}\text{O}$) trends when including either (A) all datapoints, including high-resolution and low-resolution sampling or (B) only datapoints representing high-resolution sampling. The data depicted in (A) represents the same data presented in Figure 2 of the manuscript. Blue symbols represent data collected by the authors, orange symbols represent data from Hall et al. (2018), and green symbols represent data from Petersen et al. (2016). Closed symbols represent high-resolution sampling and open symbols represent low-resolution sampling. Vertical black lines in all plots represent a LOESS curve with a span of 0.25, and the grey area represents the LOESS curve's window of error.

References

- Brand, U., and Morrison, J.O., 1987, Diagenesis and pyritization of crinoid ossicles: *Canadian Journal of Earth Sciences*, v. 24, p. 2486–2498, doi:10.1139/e87-233.
- Cochran, J.K., Kallenberg, K., Landman, N.H., Harries, P.J., Weinreb, D., Turekian, K.K., Beck, A.J., and Cobban, W.A., 2010, Effect of diagenesis on the Sr, O, and C isotope composition of late Cretaceous mollusks from the Western Interior Seaway of North America: *American Journal of Science*, v. 310, p. 69–88, doi:10.2475/02.2010.01.
- Dutton, A.L., 2003, Extracting paleoenvironmental records from molluscan carbonate [Ph.D.]: University of Michigan, 305 p.
- Ellis, N.M., and Tobin, T.S., 2019, Evidence for seasonal variation in $\delta^{13}\text{C}$ and $\delta^{18}\text{O}$ profiles of *Baculites* and implications for growth rate: *Palaeontology*, p. 1–16, doi:10.1111/pala.12416.
- Kim, S.-T., O'Neil, J.R., Hillaire-Marcel, C., and Mucci, A., 2007, Oxygen isotope fractionation between synthetic aragonite and water: Influence of temperature and Mg^{2+} concentration: *Geochimica et Cosmochimica Acta*, v. 71, p. 4704–4715, doi:10.1016/j.gca.2007.04.019.
- Knoll, K., Landman, N.H., Cochran, J.K., Macleod, K.G., and Sessa, J.A., 2016, Microstructural preservation and the effects of diagenesis on the carbon and oxygen isotope composition of Late Cretaceous aragonitic mollusks from the Gulf Coastal Plain and the Western Interior Seaway: *American Journal of Science*, v. 316, p. 591–613, doi:10.2475/07.2016.01.
- Morrison, J.O., and Brand, U., 1986, Paleocene #5. Geochemistry of recent marine invertebrates: *Geoscience Canada*, v. 13, p. 237–254.
- Moss, D.K., Ivany, L.C., Silver, R.B., Schue, J., and Artruc, E.G., 2017, High-latitude settings promote extreme longevity in fossil marine bivalves: *Paleobiology*, v. 43, p. 365–382, doi:10.1017/pab.2017.5.
- Petersen, S.V., Dutton, A., and Lohmann, K.C., 2016, End-Cretaceous extinction in Antarctica linked to both Deccan volcanism and meteorite impact via climate change: *Nature Communications*, v. 7, p. 1–9, doi:10.1038/ncomms12079.